OPEN ACCESS

Effect of Ionomer-to-Carbon Ratio on PEMFC Carbon Corrosion: An Electrochemical Study

To cite this article: Sebastian Raab *et al* 2025 *J. Electrochem. Soc.* **172** 114508

Journal of The Electrochemical Society, 2025 **172** 114508

Effect of Ionomer-to-Carbon Ratio on PEMFC Carbon Corrosion: An Electrochemical Study

Sebastian Raab,[1] Ayon Karmakar,[2] Po-Ya Abel Chuang,[2,*,z] and André Weber[1,*,z]

[1]*Institute for Applied Materials—Electrochemical Technologies (IAM-ET), Karlsruhe Institute of Technology (KIT), Karlsruhe, 76131, Germany*
[2]*Department of Mechanical Engineering, University of California, Merced, California 95343, United States of America*

This study investigates the effect of the ionomer-to-carbon (I/C) weight ratio in polymer electrolyte membrane fuel cell (PEMFC) cathode catalyst layers (CCLs) on carbon corrosion during high-potential accelerated stress tests (ASTs). Membrane electrode assemblies (MEAs) with I/C ratios of 0.5, 0.85, and 1.2 were analyzed using polarization curves, cyclic voltammetry, limiting current measurements, and electrochemical impedance spectroscopy. Impedance data analysis, based on distribution of relaxation times and transmission line modeling, showed that higher I/C ratios (0.85 and 1.2) exhibit superior beginning-of-life (BoL) performance due to lower ionic resistance in the CCL. However, the MEA with a lower I/C ratio (0.5) exhibited a performance improvement of up to 35% during initial AST cycles and enhanced carbon corrosion resistance. Compared to BoL, performance improved significantly due to a 28%–46% reduction in charge transfer resistance and a 91% reduction in ionic resistance. These findings emphasize the trade-off between BoL performance and long-term durability when determining the optimal I/C ratio. They also underscore the need for further investigation into how the I/C ratio influences CCL structure and electrochemistry. Optimizing the I/C ratio has the potential to substantially improve PEMFC electrode performance and durability, guiding the design of more resilient catalyst layers.
 [DOI: 10.1149/1945-7111/ae1b3d]

Manuscript submitted July 25, 2025; revised manuscript received September 30, 2025. Published November 18, 2025.

Supplementary material for this article is available online

The future success of polymer electrolyte membrane fuel cells (PEMFCs) is strongly dependent on further improvements in durability and efficiency, as well as cost reductions.[1] One particularly critical operating condition for PEMFC systems is the start-up/shut-down (SU/SD) process. Here, high potentials can occur locally in the cathode catalyst layer (CCL) due to a hydrogen-oxygen front at the anode, leading to corrosion of the carbon support structure within the cathode catalyst layer.[2–5] The CCL corrosion occurs due to carbon oxidation by water:[4]

$$C + 2H_2O \rightarrow CO_2 + 4H^+ + 4e^-;\ E_0 = 0.207\ V\ vs\ RHE \quad [1]$$

Severe carbon corrosion can induce changes in the electrode microstructure, porosity, thinning of the catalyst layer, and ionomer redistribution.[6,7] Additionally, carbon corrosion can alter the hydrophobicity of the carbon surface,[4,6] leading to water management issues within the MEA.[6,8] These combined adverse effects can significantly decrease the performance and lifetime of PEMFC systems. The severity of the carbon corrosion can be affected by the intrinsic material properties of the catalyst layer, carbon support, catalyst layer composition, platinum/ionomer distribution on the carbon surface, and operating conditions such as voltage, holding time, humidity, and temperature.[9,10]

The main components of PEMFC electrodes are the catalyst particles, the structural carbon support, and the ionomer. Catalyst particles, just a few nanometers in size, are anchored to the electron-conducting carbon support, which features a porous structure to facilitate transport of the gas reactants, oxygen, and hydrogen. The proton-conducting ionomer covers the platinum particles and carbon structure, forming the interface of ionomer, carbon, and catalyst, known as the triple-phase boundary (TPB), where electrochemical reactions occur. The ionomer-to-carbon (I/C) weight ratio is a critical parameter that significantly affects the electrode's microstructure, performance, and durability.[11–14] A high I/C ratio improves protonic conductivity[15] but can hinder oxygen transport to reactive sites.[16] Conversely, a low I/C ratio may lead to insufficient ionomer coverage, reducing proton conductivity and promoting local non-uniform current distribution and thermal stress on the carbon support. The optimal I/C ratio also depends on factors such as the catalyst layer thickness,[11] catalyst loading,[17] and gas humidity.[18–20] Given the unavoidable and harsh operation conditions of PEMFCs, such as hydrogen starvation or start-up/shut-down operations, a fundamental understanding of the I/C ratio's impact on carbon corrosion is essential. Optimizing the I/C ratio is crucial for balancing performance and durability, thereby enhancing catalyst layer resilience and extending overall system efficiency and lifetime.

Several studies have analyzed the influence of the I/C ratio on beginning-of-life (BoL) performance under various operating conditions,[12,15,17,21–26] its impact on catalyst layer degradation,[19,27–29] and catalyst layer morphology.[30] Only a few publications have focused on the influence of the I/C ratio on carbon corrosion.[8,31,32] Young et al.[8] have analyzed the carbon corrosion behavior of CCLs with cathode I/C ratios of 0.3 and 0.49 (23/33 wt% ionomer) using a graphitic carbon-supported platinum (50 wt% Pt/C) during potential cycling accelerated stress tests (ASTs) (0.1–1.5 V, H_2/N_2). They concluded that the rate of carbon loss was independent of the ionomer or catalyst content but reported a drastic CCL thinning (15 to 5 μm). Babu et al.[32] have examined the carbon corrosion behavior by applying high-potential cycling ASTs (1.0–1.5 V, H_2/N_2) to various CCL material combinations. They observed that the cumulative percentage of lost carbon is independent of catalyst type (Pt/PtCo), catalyst loading, I/C ratio, and equivalent weight, but is strongly affected by the carbon support type (HSAC/graphitized carbon). Alink et al.[31] identified an optimal cathode I/C ratio of 0.7–0.8 based on the BoL performance and investigated the effects of high-potential cycling (0.6–1.2 V, H_2/N_2) on various cathodes with I/C ratios ranging from 0.29 to 0.86. Their study revealed that high-potential cycling led to performance improvements, particularly at lower cathode I/C ratios. The performance enhancement was attributed to improved proton conductivity within the bulk CCL and at the CCL-membrane interface. As possible underlying mechanisms, they proposed an ionomer redistribution within the CCL and changes in carbon wettability.

Previous studies examining the impact of the I/C ratio on carbon corrosion in PEMFCs have yielded conflicting results, with some indicating that carbon corrosion is independent of the I/C ratio, while

*Electrochemical Society Member.
zE-mail: abel.chuang@ucmerced.edu; andre.weber@kit.edu

others suggest a significant influence related to catalyst type, loading, and operational conditions. Additionally, existing literature often lacks detailed electrochemical characterization under conditions representative of start-up/shut-down events. To address this gap, this study aims to systematically investigate how varying the cathode catalyst layer I/C weight ratio can influence carbon corrosion behavior in PEMFCs. Specifically, we hypothesize that optimizing the I/C ratio can improve the tradeoff between initial performance and long-term durability, particularly under accelerated corrosion conditions mimicking realistic start-up/shut-down scenarios.

In this study, the effect of the cathode catalyst layer I/C ratio on carbon corrosion behavior during high-potential cycling ASTs (1.0–1.5 V, H_2/N_2), based on the U.S. Department of Energy (DOE) testing protocol,[33] is analyzed. The DOE protocol is a commonly used AST designed to emulate high-potential degradation during start-up/shut-down operation.[34] The main focus of this analysis is the separation and quantification of polarization resistances by electrochemical impedance spectroscopy (EIS) under both H_2/air and H_2/N_2 conditions. The impedance data is further analyzed by the distribution of relaxation times (DRT) method, along with a physico-chemically meaningful equivalent circuit model including a transmission line model.[35] This in-operando analysis enables the separation and quantification of the resistances attributed to charge transfer, mass transport, and ionic transport in CCL. Additional diagnostic techniques, such as cyclic voltammetry (CV) and limiting current measurements, are also employed. This approach expands the understanding of the degradation mechanisms during carbon corrosion and the effect of the cathode I/C ratio, thereby enabling the development of more reliable PEMFC electrodes.

Experimental

Testing setup.—In this study, differential single cells with an active cell area of 1 cm^2 were tested. The PEMFCs were operated at high gas stoichiometries with a constant gas volume stream of 200 sccm to ensure a gradient-free environment in the gas channels. The minimum gas stoichiometry at 2 A cm^{-2} on the anode and cathode side was $\lambda_{anode} = 9.7$ and $\lambda_{cathode} = 6.1$, respectively. The anode and cathode gases were humidified by combustion humidification in two catalytic burner chambers,[36] which enables a dynamic adjustment of the gas humidity on the anode and cathode sides as well as the supply of oversaturated gases (RH >100%). Four combined humidity and temperature sensors, SHT41 (Sensirion, Staefa, Switzerland), were integrated in the gas lines before and after the cell housing to monitor the relative humidity and temperature of the inlet and outlet gases. A Zennium E potentiostat (Zahner, Kronach, Germany) was used for the electrochemical characterizations with a four-point measurement configuration. The cell housing was developed in-house[36] and allows precise adjustment of the active-area contacting pressure, which was set to 0.5 MPa for all tests. All experiments were conducted under atmospheric gas pressure. The anode and cathode flow fields consisted of a parallel channel design with a channel/rib width and a channel depth of 1 mm. To minimize the contact resistances, gold was used as the flow field material. For all tests, the gas diffusion layer (GDL) H14CX483 (Freudenberg, Weinheim, Germany) was used on the anode and cathode sides.[37]

Catalyst ink preparation and coating.—To prepare the catalyst ink, the appropriate amount of Pt/C catalyst powder (46.8 wt% on high-surface-area carbon, TEC10E50E, Tanaka Precious Metals, Japan) was first weighed into a 12 ml container. Separately, the required amount of Nafion ionomer (20 wt%, D2020, The Chemours Company, USA) was measured in a 10 ml glass vial and diluted sequentially with isopropanol (IPA) and deionized (DI) water, maintaining an IPA/water weight ratio of 1.5. The mixture was then sonicated in a bath at room temperature for 2–3 min to ensure proper mixing. Afterwards, both the catalyst powder and diluted Nafion solution were cooled in an ice bath for 20 min to prevent ignition of the Pt/C powder during ionomer addition. Then the Nafion solution was completely transferred to the Pt/C, containing 12 ml. Eight zirconia balls (~5 mm diameter) were added, and the container was sealed and mixed at 2000 rpm for 3 min using a high-shear mixer (AR-100, Thinky, Laguna Hills, USA) equipped with a 100AD-NAN-U adapter. For the anode catalyst ink, an I/C weight ratio of approximately 0.85 and a total solid content of ~14 wt% were used. For the cathode catalyst layers, three inks were prepared with I/C ratios of 0.5, 0.85, and 1.20. The catalyst layers were fabricated by coating onto 4 mil PTFE decal substrates using Mayer rods of various sizes to achieve the desired loadings. After coating, the substrates were left to dry naturally at room temperature.

Membrane electrode assembly.—Three membrane electrode assemblies with varying I/C weight ratios of the cathode catalyst layer (CCL) were tested. The specifications of the MEAs are listed in Table I. The catalyst layers and the reinforced Nafion membrane NC700 (The Chemours Company, USA) were assembled by a hot-pressing process at 130 °C and 300 psi (≈2.06 MPa) for 5 min.[38] The platinum loading of the catalyst layers was determined gravimetrically by weighing the dry catalyst layer on the decal substrate prior to transfer and calculating the platinum mass fraction from the ink solids composition (Pt wt% in Pt/C and I/C), then dividing by the coated area. The platinum loadings of the anode and cathode were 0.12 ± 0.04 mg_{pt} cm^{-2} and 0.19 ± 0.02 mg_{pt} cm^{-2}, respectively. The I/C weight ratio of the anode catalyst layer (ACL) was kept constant at 0.85, while that of the CCL was varied (I/C = 0.5/0.85/1.2). In this study, one sample with a low, medium, and high I/C ratio were tested. The electrochemically active surface area (ECSA) at BoL was estimated by using the standard hydrogen adsorption and desorption (HAD) measurement method. The measured charge per mass of platinum corresponding to the H-adsorption peak in the cyclic

Table I. Membrane electrode assembly (MEA) and gas diffusion layer (GDL) specifications of I/C ratio variation (I/C = 0.5/0.85/1.2) of the cathode catalyst layer.

Material parameter	Unit	MEA I/C-0.5 (low I/C)	MEA I/C-0.85 (medium I/C)	MEA I/C-1.2 (high I/C)
I/C weight ratio (cathode)	—	0.5	0.85	1.2
I/C weight ratio (anode)	—	0.85	0.85	0.85
Solid content (cathode)	wt%	12.5	14.1	15.6
CCL thickness (BoL)	μm	5.7	6.8	6.1
ACL thickness (BoL)	μm	3.5	4.2	5.7
Pt loading (cathode)	mg_{pt} cm^{-2}_{geo}	0.207	0.17	0.196
Pt loading (anode)	mg_{pt} cm^{-2}_{geo}	0.129	0.08	0.148
ECSA cathode (BoL)	m^2_{pt} g^{-1}_{pt}	73.2	70.6	72.4
Catalyst/Carbon	—	Tanaka TEC10E50E (Ketjenblack EC)		
CL Ionomer	—	Chemours Nafion D2020		
Membrane	—	Chemours NC700 (reinforced, 15 μm)		
Gas diffusion layer	—	Freudenberg H14CX483 with microporous layer (MPL)		

voltammograms was divided by the surface charge density of H-adsorption on polycrystalline platinum (210 μC cm^{-1}). The thickness of the cathode catalyst layer was determined via cross-sectional analysis using the digital microscope VHX-7000 system (Keyence, Osaka, Japan).

Accelerated stress test.—The applied accelerated stress test (AST) procedure was based on the protocol published by the U.S. DOE,[33] emulating start-up/shut-down conditions by applying triangular wave cycles in a voltage range of 1.0–1.5 V at a rate of 500 mV s^{-1}. The ASTs were conducted under H_2/N_2 (anode/cathode) conditions at 80 °C and 95% RH, specifically aimed to corrode the carbon support structure in the CCL. These experimental parameters were deliberately selected to simulate the realistic conditions encountered during PEMFC start-up/shut-down events. The test conditions were chosen to replicate aggressive carbon corrosion scenarios commonly observed during transient operating states, thereby enabling the identification of material-specific degradation mechanisms and ensuring the practical relevance of the findings. Prior to the initiation of the AST, multiple BoL characterizations were conducted to ensure the reproducibility and stability of the tested samples. Characterization was subsequently repeated at AST cycle intervals ranging from 10 to 300 cycles. The end of life (EoL) was defined as the point when a maximum current density of 0.475 A cm^{-2} could no longer be reached.

Electrochemical characterization.—Electrochemical characterization included a recovery procedure, polarization curves, EIS under H_2/air conditions at multiple current densities, EIS under H_2/N_2 conditions, cyclic voltammetry (CV) at both anode and cathode, and limiting current measurements using different inert gases (He/N_2). Before each electrochemical characterization, a recovery procedure was conducted, which involved reducing the cell temperature to 40 °C at 80% RH. Subsequently, the cell potential was set to 0.85 V for 5 min, 0.6 V for 10 min, and 0.3 V for 60 min for two full cycles.[39] Testing conditions such as humidity and temperature were selected based on typical automotive operating conditions. Specifically, humidity levels (70%–95%) were chosen to examine their effect on ionomer hydration and proton conductivity, a temperature of 80 °C was used to reflect realistic PEMFC operating conditions impacting reaction kinetics and carbon corrosion rates. A constant gas flow was set with a minimum gas stoichiometry of 6.1 at 2 A cm^{-2} to minimize mass transport limitations and isolate local degradation phenomena.

Electrochemical impedance spectroscopy.—Electrochemical impedance spectroscopy (EIS) was conducted using hydrogen (anode) and synthetic air (cathode) for in-operando analysis (T = 80 °C, RH = 70% sym., $p_{O2,dry}$ = 0.315, atmospheric pressure) of electrochemical resistances and loss processes. EIS was performed galvanostatically at current densities from 0.025 A cm^{-2} to the maximum current density achievable at 0.3 V (up to 2.0 A cm^{-2}). A constant reactant gas flow of 200 sccm was supplied, corresponding to high gas stoichiometries, which allows gas conversion along the gas channel to be neglected. Prior to EIS measurements, all cells were conditioned at the maximum current density reached at 0.32 V for 120 min to ensure stable operating conditions. Impedance spectra were recorded in a frequency range from 1 MHz to 500 mHz with a perturbation amplitude of 1–50 mA cm^{-2}. Polarization curves were derived from the current density and voltage during EIS measurements. The ionic resistance of the CCL was determined separately by EIS (T = 80 °C, RH = 30%) under hydrogen (anode) and nitrogen (cathode) conditions, with a reactant gas flow of 200 sccm. A holding time of 30 min was implemented prior to measurement to ensure stable operation. EIS was measured potentiostatically at 0.5 V between 500 mHz and 1 MHz, with a perturbation amplitude of 20 mV.

Impedance data analysis.—The validity of the impedance data was ensured by applying the Kramers-Kronig test.[40] The residual error for all EIS measurements was low (« 1%), indicating high data quality. To deconvolute the electrochemical processes and their characteristic time constants,[41,42] impedance spectra were analyzed by the distribution of relaxation times. The allocation of the DRT peaks to specific loss processes was achieved by a systematic variation of the operating conditions, as introduced by Heinzmann et al.[35] The resistances associated with each loss process were determined by fitting an equivalent circuit model to the EIS (H_2/air) and DRT data using a complex nonlinear least squares fit (CNLS) approximation.[43]

The cathode catalyst layer was modeled using a transmission line model (TLM), taking into account the ionic transport resistance and the charge transfer resistance at the triple phase boundary.[35,44] In series with the TLM, the membrane resistance was represented by an ohmic resistance (R_0), and the gas diffusion resistance (through the CCL, GDL, MPL) by a generalized, finite-length Warburg element (GFLW).[45] The ohmic resistance was corrected by 0.014 Ω cm^2 to account for the electrical resistance of the PEMFC setup, including housing and wiring. Overall, the TLM impedance of a porous CCL (Z_{TLM}) can be described as follows:[35,46]

$$Z_{TLM}(\omega) = \frac{\chi_1\chi_2}{\chi_1+\chi_2}\cdot\left(L+\frac{2\kappa}{\sinh\left(\frac{L}{\kappa}\right)}\right) + \kappa\cdot\frac{\chi_1{}^2+\chi_2{}^2}{\chi_1+\chi_2}\cdot\coth\left(\frac{L}{\kappa}\right) \quad [2]$$

$$\kappa = \sqrt{\frac{\xi}{\chi_1+\chi_2}} \quad [3]$$

This TLM expression considers the resistances of the ionic path χ_1 (Ω m^{-1}), the electrical path χ_2 (Ω m^{-1}), the complex TLM expression of the charge transfer resistance ξ (Ωm) between both paths, and the CCL thickness L (5.7–6.8 μm). A negligible and constant electronic resistance ($\chi_2 \approx 0$) was assumed due to the high conductivity of the carbon support in pristine electrodes.[47] However, this assumption may not be valid under severe carbon corrosion. Nevertheless, this simplification enables comparative trend analysis. The complex TLM expression of the charge transfer resistance ξ is represented by an R-Q element, considering the thickness-specific charge transfer r_{ct} (Ω m) and the characteristic time constant of the charge transfer τ_{ct} (s).[35]

$$\xi(\omega) = \frac{r_{ct}}{1+(j\,\omega\,\tau_{ct})^n} \quad [4]$$

Symmetrical cell tests (H_2/H_2 conditions) revealed a negligible polarization resistance of the hydrogen oxidation reaction on the anode (<0.011 Ω cm^2) for the given testing conditions, which is below 4% of the overall polarization resistance of the cell.[36] Thus, the anode contribution was neglected in the further analysis. The TLM parameters of the charge transfer resistance r_{ct} and ionic resistance in the CCL r_{ion} (=χ_1) are determined by fitting the ECM to the measured EIS and DRT data. The overall charge transfer resistance R_{ct} (Ω cm^2) of the cathode, with a CCL thickness L and an active cell area A (1 cm^2), was calculated according to Eq. 5.

$$R_{ct} = \frac{r_{ct}\cdot A}{L} \quad [5]$$

The theoretical ionic resistance (Ω cm^2) in the CCL can be calculated by Eq. 6.

$$R_{ion}^{theor.} = r_{ion} \cdot L \cdot A \quad [6]$$

However, the local ionic current density is not constant throughout the complete cathode catalyst layer thickness, decreasing from the membrane towards the catalyst layer surface.[44] To account for this decline, the effective ionic resistance is calculated by adding a factor of 1/3[48] to Eq. 6.

$$R_{ion}^{eff} = \frac{1}{3} \cdot r_{ion} \cdot L \cdot A \quad [7]$$

In this study, all ionic resistances in the CCL were calculated using Eq. 7. To improve readability, this value will be referred to as ionic resistance (R_{ion}) throughout this publication.

EIS under H_2/N_2 conditions.—The ionic resistance from EIS measurement under H_2/N_2 (anode/cathode) conditions was calculated by fitting the data to a modified version of the previously described ECM/TLM. The modification included the removal of the charge transfer resistance (r_{ct}) from the TLM described in Eq. 4, as no charge transfer takes place under H_2/N_2 conditions.

Cyclic voltammetry.—Cyclic voltammetry (CV) was used to determine the ECSA, roughness factor (RF), and double-layer capacitance (DLC) of the CCLs. CV was conducted at 50 °C and 95% RH between 0.05 V and 1.2 V for 10 cycles with scan rates of 50, 150, and 400 mV s^{-1}, respectively. The gases of 200 sccm (H_2) and 50 sccm (N_2) were supplied for 5 min before the start of the measurement. Shortly before the measurements, the N_2 flow was switched off. The roughness factor was determined using the standard HAD (hydrogen adsorption and desorption) method by integrating the hydrogen adsorption area between 0.05 V and 0.4–0.5 V, and correlating it with the geometrical MEA area (1 cm^2). Furthermore, the hydrogen crossover current density was calculated from the cyclic voltammograms.

Limiting current measurements.—Limiting current measurements were conducted with two inert gases (He/N_2) to separate the molecular diffusion resistance (GDL substrate and gas channel) from the sum of the Knudsen (MPL and CCL) and film diffusion resistance (ionomer and water films). Measurements were conducted at oxygen concentrations of 1%, 2%, 3%, 4%, and 5% in the respective inert gas on the cathode side. The potential was decreased from 0.4 V to 0.1 V in 20 mV steps, with a holding time of 1 min at each potential. The limiting current value was determined at 0.12 V. All measurements were conducted at 80 °C, 95% RH, and a constant gas flow of 200 sccm at the anode and cathode. Before each measurement, the operating conditions were held for 5 min to ensure stable operation. The separation of molecular and Knudsen/film diffusion resistances by Eqs. S1–S4 is detailed in the supplementary material.[49,50]

The described characterization techniques and modeling approaches were utilized to analyze the influence of the cathode catalyst layer I/C ratio on the carbon corrosion behavior and cell performance during high-potential ASTs. All samples were subjected to the same characterization and carbon corrosion AST procedures. To strengthen these electrochemical interpretations, future studies should incorporate microstructural analysis, such as scanning electron microscopy (SEM) or transmission electron microscopy (TEM).

Results and Discussion

Initially, we present the electrochemical BoL characterization results, establishing the reference state for all subsequent analyses.

Beginning-of-life (BoL) characterization.—The polarization and power curves (Fig. 1a) show that I/C-1.2 and I/C-0.85 have similar overall **BoL performances**, with power densities at 0.6 V of 0.687 W cm^{-2} and 0.689 W cm^{-2}, respectively. In contrast, I/C-0.5 exhibits a significantly lower BoL performance of 0.239 W cm^{-2}. The lower performance of I/C-0.5 is likely a result of low platinum utilization due to poor proton conduction in the CCL.[51] The difference in BoL performance does not correlate with the differences in **cathode catalyst layer loading**, which vary between 0.17 mg_{pt} $cm^{-2}{}_{geo}$ (medium I/C), 0.196 mg_{pt} $cm^{-2}{}_{geo}$ (high I/C), and 0.207 mg_{pt} $cm^{-2}{}_{geo}$ (low I/C). For the catalyst/carbon type used in this study (TEC10E50E, 46 wt% Pt/C), previously reported optimal cathode I/C ratios include 0.75,[52] 0.72,[16] and 1.0.[27] For other high-surface-area carbon supports, optimal I/C values vary depending on catalyst and operating conditions, for example, 0.71 under wet conditions and 1.11 under dry conditions for a 40/60 wt% Pt catalyst,[17] and 1.0 (30 wt% ionomer) for a 57 wt% Pt catalyst (Hispec 9100).[28] While Song et al.[53] reported an independence of the optimal I/C ratio from operating conditions (temperature, RH) and platinum loading (0.1–0.37 mg_{pt} $cm^{-2}{}_{geo}$), other studies highlight the dependency on catalyst type, loading, and operating conditions, especially the gas humidity.[17]

The **electrochemically active surface area** (Table SII) determined from the cyclic voltammograms (Fig. 1c) at the first BoL characterization was similar for all three samples (70.6–73.2 m^2 $g^{-1}{}_{pt}$). These values were slightly higher than literature values of 46 wt% Pt catalyst (TEC10E50E), which range from 35–66 m^2 $g^{-1}{}_{pt}$ (I/C = 0.16–1.14)[16] to 57–59 m^2 $g^{-1}{}_{pt}$ (I/C = 0.6–0.9).[53] Note that the ECSA value can be influenced by differences in preparation processes,[54] catalyst layer thickness and loading,[55] measurement conditions,[56] and manufacturing procedure.[57,58] In the literature, an increase in ECSA with increasing I/C ratios has been reported,[16,52,59–61] with a plateau observed at I/C ratios larger than 0.625 (corresponding to 20 wt% Nafion)[60] and 0.41.[16] This plateau is attributed to the complete formation of continuous proton transport pathways at higher ionomer contents. In contrast, low I/C ratios can lead to low ECSA due to poor ionomer coverage on the Pt/C surface[16,60] and the disconnection of active sites from the proton conduction network.[59] Additionally, it has been reported that a large fraction of platinum can reside in mesopores, which are inactive under dry conditions but become activated at high RH due to the presence of liquid water.[61] The high RH during CV measurements (95%) could have led to an activation of platinum within mesopores, contributing to a high ECSA of the low I/C ratio sample.

The **double-layer capacitance (DLC)** of the CCL (Table SII), determined by CV, can be directly correlated with the ionomer distribution,[62] which in turn depends on pore size distribution, surface area, and the utilized carbon type.[63] At low RH, the DLC primarily represents the platinum-ionomer and carbon-ionomer interfaces, while at high RH, additional contributions arise from the platinum-water and carbon-water interfaces.[62] The significantly lower DLC of the low I/C sample, despite a comparable ECSA and similar CCL humidification, suggests that the platinum-ionomer and carbon-ionomer interface area is significantly reduced. This reduction could be attributed to the combination of inhomogeneous ionomer distribution and low ionomer coverage.[62]

The **Nyquist plots** of the EIS data (Fig. 1b) show that all samples have similar high-frequency resistances (HFR), indicating that the variation of the I/C ratio does not affect the membrane conductivity[17] and the contact resistances. All spectra show similar low-frequency behavior, whereas the main differences are observed at intermediate frequencies. The total resistance is largest for I/C-0.5 (0.55 Ω cm^2), followed by I/C-0.85 (0.28 Ω cm^2) and I/C-1.2 (0.26 Ω cm^2). The higher polarization resistance of I/C-0.5 is the main contributor to its lower performance observed in Fig. 1a.

The **distribution of relaxation times** approach was employed to deconvolute the individual loss processes (Fig. 1d) contributing to the overall polarization resistance. Each peak (P1–P5) represents a distinct loss mechanism, while the area under the peak corresponds to its associated resistance. Heinzmann et al.[35] attributed the DRT peaks to the mass transport resistance (P1) in the low-frequency range (2–10 Hz), the charge transfer resistance of the oxygen

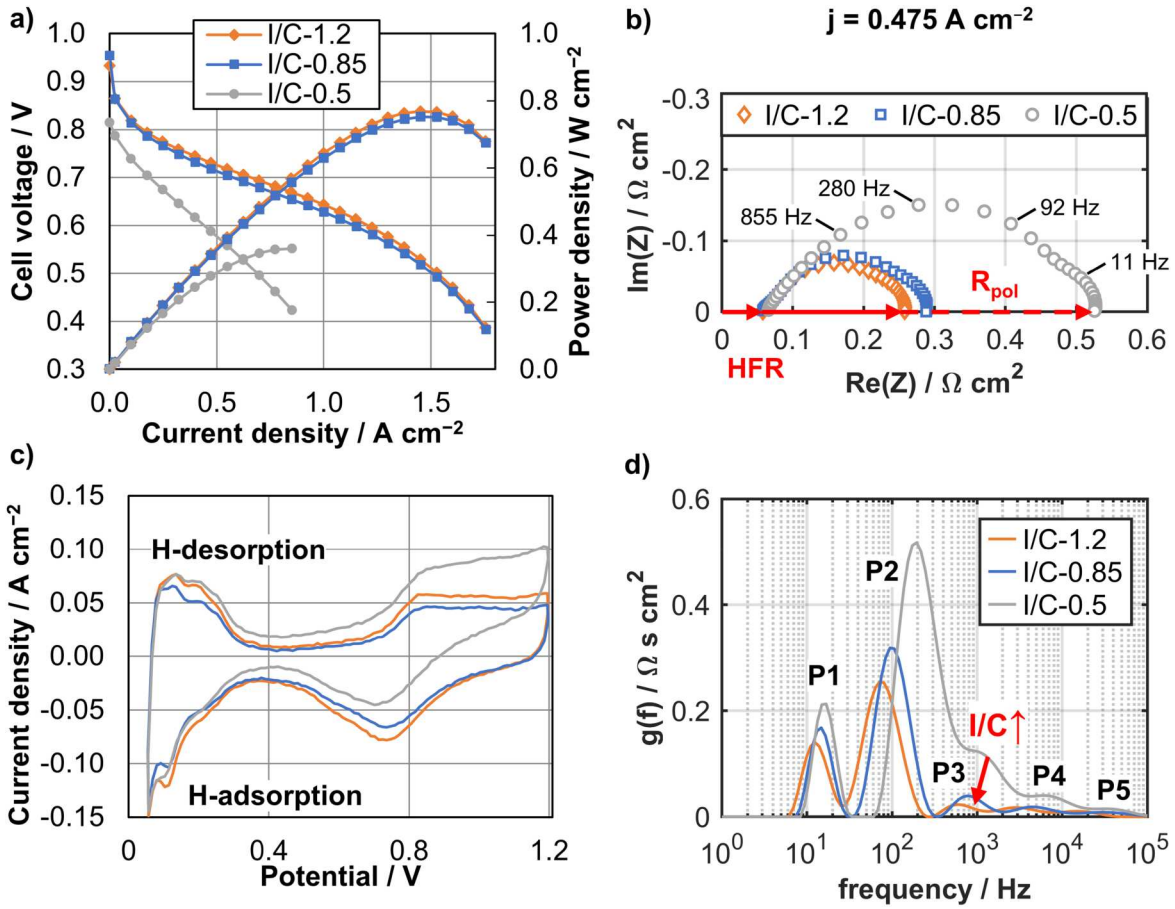

Figure 1. Beginning-of-life (BoL) characterization of three I/C ratio (0.5/0.85/1.2) samples by polarization/power curves (T = 80 °C; RH = 70% sym.; $p_{O2,dry}$ = 0.315 atm; $\dot{V}$ = 200 sccm) (a), electrochemical impedance spectra under H_2/air conditions at 0.475 A cm^{-2} (b), cyclic voltammetry of the cathode (T = 50 °C; RH = 95% sym.; $\dot{V}$ = 200 sccm) (c), and distribution of relaxation times (DRT) (d).

reduction reaction (ORR) (P2) at medium frequencies (20–200 Hz), and the ionic resistance in the cathode catalyst layer as well as the overlapping anode processes such as the hydrogen oxidation reaction (HOR) (P3–P5) in the high-frequency range (300 Hz–30 kHz). Due to the nature of the spatially distributed processes in the finite-length Warburg element and TLM, the DRT of such equivalent circuit elements consists of a main peak and a number of smaller sub-peaks at higher frequencies.[64] Thus, a direct quantification of the polarization resistance contribution from the area underneath the DRT peak is not meaningful, and appropriate ECM elements considering the coupling of transport and reaction have to be applied in complex nonlinear least squares fitting. Nonetheless, the DRT provides a meaningful qualitative visualization of underlying dependencies.

The **ORR charge transfer resistance** (DRT peak P2) at BoL increases with decreasing I/C ratio. It has been reported that the charge transfer resistance is directly affected by the ECSA, porosity, and thickness of the CCL.[60,65] Okumura et al.[16] reported increased activation overpotential at both low (I/C = 0.16) and high (I/C = 1.14) Nafion contents, attributing it to insufficient ionomer coverage or excessive ionomer blocking active sites, respectively, leading to reduced Pt utilization. Therefore, the significantly higher charge transfer resistance at a low I/C ratio can be attributed to the insulation of platinum particles from the proton-conducting network, either due to insufficient ionomer coverage of the Pt/C surface[62] or the placement of platinum particles within carbon micropores.[66] Ott et al.[67] reported that 85%–90% of platinum particles (Pt/KB, I/C = 0.66) were located on the exterior surface of the carbon support, regardless of the high-surface-area carbon type. However, platinum particles, which are not in contact with the ionomer, can remain inactive under low RH[20,66] conditions but can be connected to the proton-conducting network through liquid water formation at high RH. The difference in RH between EIS (70%) and CV (95%) measurements may explain the observed discrepancy between the similar ECSA values at BoL and the significantly different charge transfer resistance (R_{ct}) for different I/C ratios (Table SII).

The **ionic resistance of the CCL** (DRT peak P3) was identified as one of the main reasons for the reduced BoL performance of the low I/C sample. At BoL, the ionic resistance of the low I/C sample was significantly higher (0.315 Ω cm^2 at 0.475 A cm^{-2}) compared to the medium (0.051 Ω cm^2) and high I/C (0.021 Ω cm^2) samples. The increase in ionic resistance with decreasing I/C ratio has been reported in several publications.[15,29,59,61] The elevated ionic resistance of the low I/C sample is likely due to insufficient ionomer coverage[62] and the formation of disconnected ionomer domains on the mesoporous Pt/C surface.[61] The small difference in ionic resistance between the medium and high I/C samples can be explained by the complete formation of a well-connected proton-conducting network, which has been reported to form at I/C ratios larger than 0.6[15] and 1.07.[60] Alink et al. [31] reported a higher proton resistance of the bulk CL and the CL-membrane interface for low I/C ratios, resulting in the primary reaction zone shifting towards the membrane-CL interface. While this shift reduces the length of protonic pathways, it also increases the oxygen diffusion path through the catalyst layer, thereby increasing the mass transport resistance.

The **mass transport resistance** (DRT peak P1) rises with decreasing I/C ratio. It has been widely reported that an increase in the I/C ratio leads to a decrease in CCL porosity and mean pore size, coupled with an increase in tortuosity,[2,68–70] leading to an increase in mass transport resistance.[16,52,59] Contrarily, Okumura et al.[16] observed

an increase in concentration overvoltage at low I/C ratios (0.16) at 0.2 A cm^{-2}, but did not further discuss this finding. Yakovlev et al.[59] also reported the largest total gas transport resistance for low (0.1) and high (1.0) I/C ratios at all tested current densities. Besides the mentioned microstructural parameters (porosity, tortuosity, and pore size), the ionomer layer characteristics can also influence the mass transport resistance. Low I/C ratios can lead to lower ionomer layer thickness and coverage,[62] which can result in a high proton transport resistance at the CL-membrane interface. This can shift the primary reaction zone closer to the membrane-CL interface,[31] leading to a longer oxygen diffusion pathway within the catalyst layer. Moreover, this effect could be amplified by additional water generation, inhibiting oxygen transport. It is hypothesized that the rising mass transport resistance with decreasing I/C ratio stems from a shift of the primary reaction towards the CL-membrane interface, increasing the oxygen diffusion pathway. Furthermore, the low I/C sample had the greatest increase in mass transport resistance with increasing current densities (Fig. S2), which can be attributed to pore blockage from condensed water.

Limiting current measurements enable a deeper understanding of the origin of mass transport resistance by separating and quantifying the contributions of Knudsen/film diffusion and molecular diffusion. Oh et al.[71] analyzed the oxygen transport resistance under high relative humidity (RH = 90%), attributing the total resistance to the MPL (36%), catalyst layer (30%), ionomer film (18%), and GDL substrate (16%). At BoL, the **molecular diffusion resistance** among the different I/C samples does not differ significantly (Table SII). As molecular diffusion mainly takes place in the GDL and, to a lesser extent, the MPL and catalyst layer,[71] the influence of the I/C ratio on the larger pores, which mainly contribute to molecular diffusion rather than Knudsen diffusion, in these three layers can be neglected at BoL. In the literature, an increase in **Knudsen diffusion resistance** with increasing ionomer content has been attributed to a decrease in mean pore diameter and porosity.[16,52,59] The **ionomer film resistance** rises with higher I/C ratios due to complete ionomer coverage, leading to an increase in ionomer layer thickness covering the Pt surface.[59,60] On the other side, Ott et al.[67] reported an inhomogeneous distribution of ionomer for Pt/KB (I/C = 0.66), with the Pt-ionomer interface resistance playing a larger role than the Knudsen diffusion in pressure-independent mass transport resistance. They concluded that the inhomogeneous ionomer distribution leads to a locally reduced oxygen resistance at the Pt-ionomer interface, as significant portions of the platinum surface are not covered by ionomer. Simultaneously, Knudsen resistance increases due to partial micro- and mesopore blockage and ionomer accumulation around primary carbon particles.[72] In Fig. 7b, the **Knudsen and film diffusion resistance** at BoL of all three samples only differ slightly. This observation may be explained by a trade-off between lower Knudsen diffusion resistance and elevated ionomer film resistance due to inhomogeneous ionomer distribution with decreasing I/C ratios. However, since the individual contributors were not separately resolved in this work, these interpretations remain hypothetical.

Evolution of cell voltage with carbon corrosion.—In Fig. 2, the medium (I/C-0.85) and high (I/C-1.2) I/C ratio samples show similar trends of the cell voltage evolution across all three current densities, with degradation rates increasing over the course of AST cycles. In contrast, the low I/C sample (I/C-0.5) initially shows improved performance up to 500 AST cycles, followed by a sharp voltage decline. The complete set of polarization curves for all three samples throughout the ASTs is presented in Fig. S4.

During high-potential cycling, the low I/C sample demonstrated superior carbon corrosion durability, outperforming the medium and high I/C samples. The **total number of high-potential cycles** required to reach the EoL criteria ($j_{max} < 0.475$ A cm^{-2}) was highest for the low I/C sample (1700 cycles), compared to the medium (590 cycles) and high I/C samples (800 cycles). This durability was reflected in the **power density** degradation rates at 0.475 A cm^{-2}, which were lowest for I/C-0.5 (−55% per 1000 cycles), followed by I/C-1.2 (−66% per 1000 cycles) and I/C-0.85 (−106% per 1000 cycles). The elevated degradation rate of I/C-0.85 could have been induced by the lower platinum loading compared to the other samples.[73] The notable initial performance improvement of the low I/C sample in the first 500 AST cycles might have resulted from a beneficial redistribution of the ionomer within the CCL and/or improved proton connectivity between the membrane and the CCL ionomer.[31] Alink et al.[31] reported an increase in performance at low I/C ratios (0.29–0.56) during high-potential cycles with a simultaneous decrease in ECSA and DLC. In our study, the performance improvement was more pronounced at lower I/C ratios, attributed to a significant enhancement in proton conductivity. Considering only voltage degradation does not allow for a comprehensive assessment of the effect of the cathode I/C ratio on carbon corrosion during accelerated stress tests.

One of the main contributors to the performance loss during AST was the increase in **ohmic resistance**. At BoL, all samples had similar values (0.039–0.040 Ω cm^2), indicating that the membrane properties were not affected by the I/C ratio. During high-potential cycling, the open circuit voltages and hydrogen crossover currents of all I/C samples remain relatively stable (Fig. S7a), while their ohmic resistances increase steadily. The increase in ohmic resistance can therefore be attributed to a decline in electrical conductivity in the CCL[8,74] due to the severe corrosion of the carbon structure. In addition to electronic resistance, part of the apparent resistance rise likely originates from the proton-transport resistance in the cathode catalyst layer, which becomes evident in the high-frequency region. The assumption of constant electronic conductivity in severe corrosion conditions, though common in the literature, warrants careful reconsideration. Future work should experimentally validate this assumption or investigate potential conductivity changes under extended corrosion scenarios. Even within the first 500 cycles, the low I/C sample demonstrated a gradual increase in ohmic resistance, but with a significantly lower degradation rate compared to the other samples. The results suggest that the initial performance enhancement was not due to improvements in ohmic resistance but was driven by other electrochemical processes, which will be discussed in the following sections.

Before the start of the first ASTs, several BoL characterizations were performed to ensure cell stability and reproducibility. In Fig. S3, all samples exhibited stable cell voltages before the initiation of AST cycles. I/C-0.85 and I/C-1.2 showed a progressive decline in performance with the AST cycles, while I/C-0.5 demonstrated an initial increase in cell voltage up to 93 h (500 cycles), followed by a subsequent decrease. This behavior clearly indicates that the early-state performance improvement of I/C-0.5 was triggered by high-potential cycling. To support these findings and identify the origin of the initial voltage increase, while linking it to specific loss processes, an electrochemical analysis was conducted using electrochemical impedance spectroscopy combined with additional electrochemical analysis techniques.

Electrochemical impedance spectroscopy and distribution of relaxation times.—To isolate and quantify the loss processes contributing to changes in cell voltage during carbon corrosion AST cycles, EIS was performed under H_2/air conditions at multiple current densities. EIS enables a direct quantification of the ohmic and polarization resistance. Additionally, the distribution of relaxation times approach and an equivalent circuit model (ECM) were utilized to further separate and quantify the charge transfer resistance, ionic resistance in CCL, and mass transport resistance.

In the following sections, the ECM fitting results from the EIS measurements at 0.475 A cm^{-2}, as well as the results of additional electrochemical measurement techniques, such as cyclic voltammetry, limiting current measurements, and EIS under H_2/N_2 conditions, are discussed.

In Fig. 3a, the impedance spectra of the high I/C sample (I/C-1.2) up to 800 AST cycles are shown. The high-frequency resistance

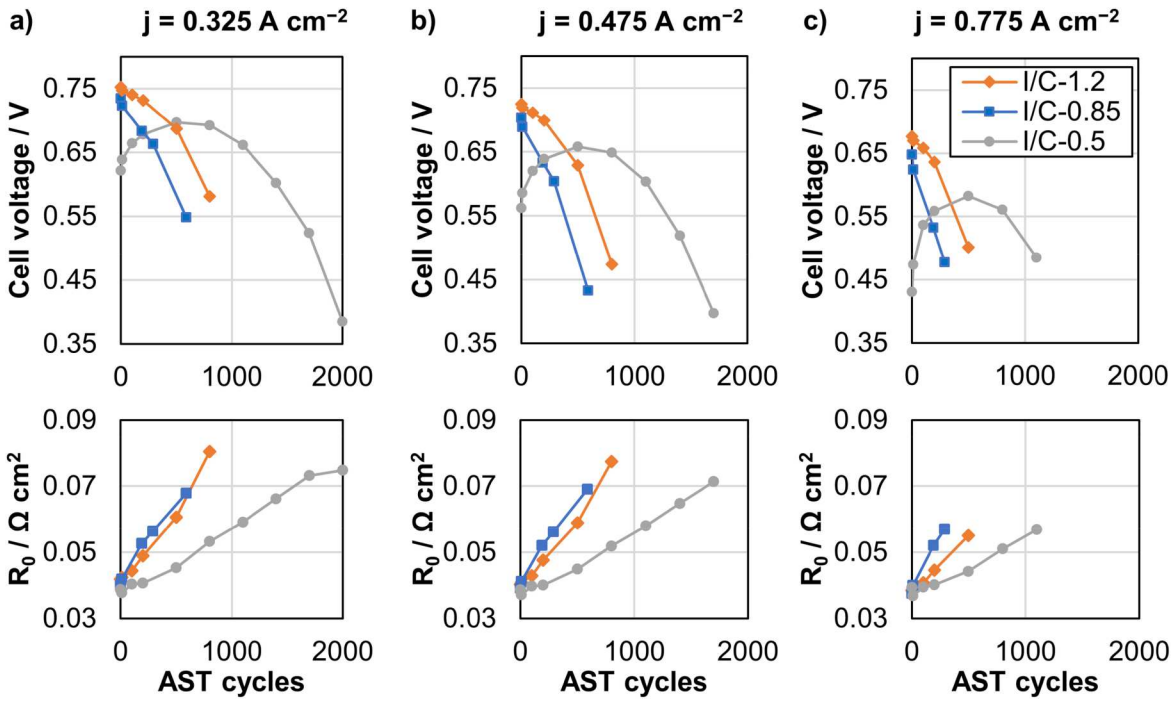

Figure 2. Cell voltage and ohmic resistance of the I/C ratio samples (0.5/0.85/1.2) at 0.325 A cm^{-2} (a), 0.475 A cm^{-2} (b), and 0.775 A cm^{-2} (c) as a function of AST cycles (T = 80 °C; RH = 70% sym.; $p_{O2,dry}$ = 0.315 atm; $\dot{V}$ = 200 sccm).

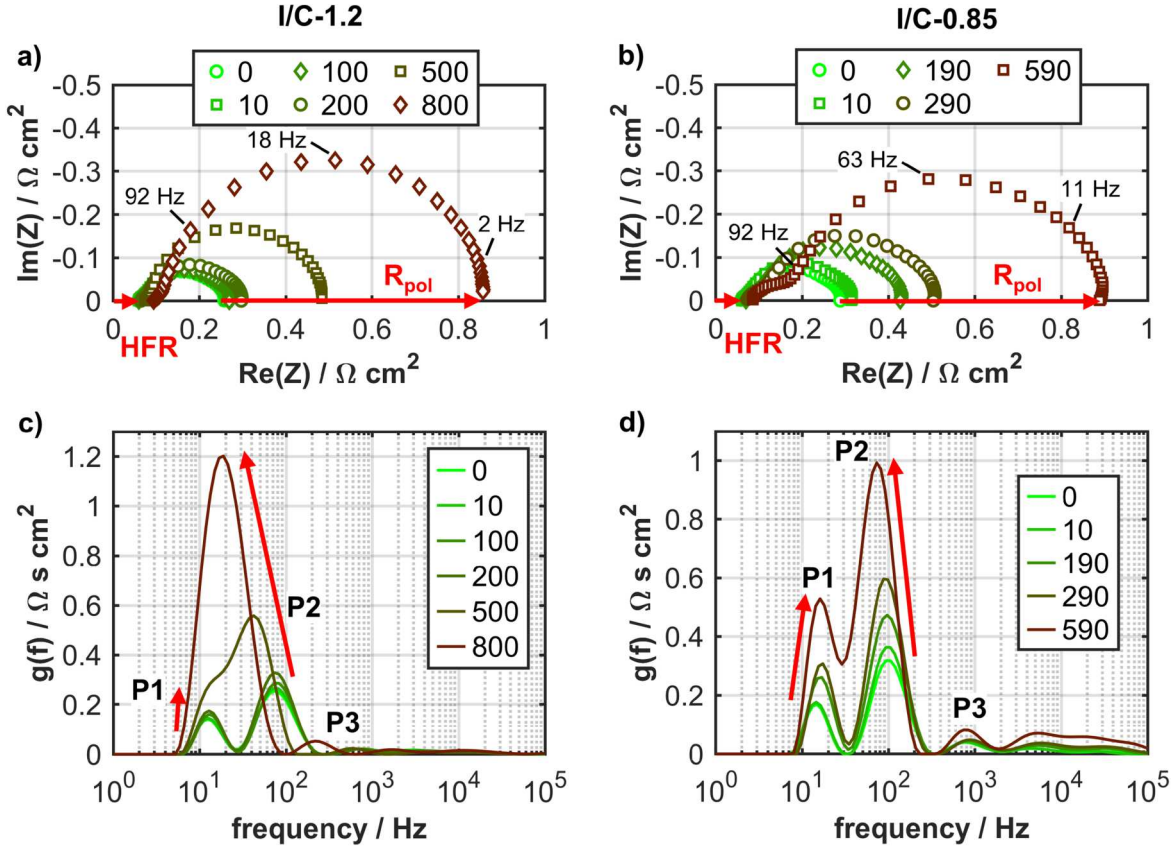

Figure 3. EIS (Nyquist Plot) and distribution of relaxation times (DRT) of I/C-1.2 (a,c), and I/C-0.85 (b,d) at 0.475 A cm^{-2} after various AST cycles (T = 80 °C; RH = 70% sym.; $p_{O2,dry}$ = 0.315 atm; $\dot{V}$ = 200 sccm).

(HFR), polarization resistance (R_{pol}), and DRT peaks (Fig. 3c) remain stable until 200 AST cycles, after which they increase significantly. Based on the DRT analysis, the substantial increase in R_{pol} can be attributed to a significant increase in charge transfer resistance (P2), accompanied by a decrease in relaxation frequency. The mass transport peak (P1) is increasingly overlapping with the

charge transfer peak (P2), making the separation of the two resistances challenging. To overcome this issue, the quantification by ECM fittings was validated by cyclic voltammetry and limiting current measurements, as discussed in the following sections.

In Fig. 3b, the medium I/C sample (I/C-0.85) reached a maximum of 590 AST cycles at 0.475 A cm^{-2}. High-frequency and polarization resistance increased sharply with the AST cycles (Fig. 3b). In the DRT analysis (Fig. 3d), a pronounced increase of the mass transport (P1) and charge transfer (P2) peaks can also be observed. In comparison to the I/C-1.2 sample, the relaxation frequency of P2 decreases to a minor extent, while P1 and P2 are clearly separated over the entire test duration.

Since the low I/C sample (I/C-0.5) showed a distinct behavior before (Figs. 4a, 4c) and after 500 cycles (Figs. 4b, 4d), the EIS and DRT at 0.475 A cm^{-2} of these two phases are plotted separately.

Different from the other two samples, the impedance spectra of I/C-0.5 show a decreasing polarization resistance in the first 500 AST cycles (Fig. 4a). Analysis using the DRT (Fig. 4c) indicates that this reduction is mainly associated with processes >100 Hz, especially the charge transfer (P2) and ionic resistance in the CCL (P3), suggesting modifications in protonic transport pathways in the cathode catalyst layer, which affect the charge transfer (P2) as more reaction sites become accessible via the improved ionomer network. Although these two peaks partially overlap, a clear decrease in both can be observed. After 500 cycles, the charge transfer and ionic resistance peak values are comparable to the BoL values of the medium and high I/C samples (Fig. S6). The mass transport resistance (P1) does not change significantly in the first 500 cycles. It is hypothesized that the high-potential cycling may have induced a beneficial redistribution of ionomer within the CCL of the low I/C sample. After 500 cycles, both polarization and ohmic resistance increase, a trend observed for all samples, due to the continuous carbon corrosion (Fig. 4b). Similar to the I/C-0.85 and I/C-1.2 samples, the increase in polarization resistance is mainly driven by a rise in charge transfer resistance (P2), which is increasingly overlapping the mass transport peak (P1) at high AST cycle numbers.

The **distribution of relaxation times** analysis for all samples reveals a shift of the characteristic frequency of the charge transfer peak (P2) toward lower frequencies. This behavior can be attributed to the structural deformation of the carbon support, the formation of oxygen-containing functional groups, and water management issues.[75] Notably, despite the reduction in charge transfer resistance and improvement in performance, the charge transfer peak (P2) in the low I/C sample still exhibited a similar shift towards lower frequencies during the first 500 AST cycles, suggesting that the same mechanisms remain active.

The ECM fitting results are summarized in Fig. 8 for all three samples. This includes the series resistance R_0, ORR charge transfer resistance R_{ct}, ionic resistance R_{ion} in the CCL, and mass transport resistance R_{mt} evaluated from P1. In the following, these impedance-based values will be discussed and correlated to other measurement results.

Charge transfer resistance and cathode roughness factor.—In Fig. 5, the evolution of the charge transfer resistance at 0.475 A cm^{-2} and the cathode roughness factor normalized to the beginning-of-test (BoT) values are shown as a function of the AST cycles. As several electrochemical characterizations (polarization curves, EIS, cyclic voltammetry, and limiting current measurements) were conducted before the initiation of the AST, BoT refers to the last characterization before the start of the AST. The plots of the cyclic voltammograms for all three samples, the evolution of the absolute values of the cathode roughness factor, and the cathode ECSA are presented in the supplementary material (Figs. S5 and S9).

The **charge transfer resistance** increased similarly for the medium and high I/C samples with the number of AST cycles. In contrast, the charge transfer resistance of the low I/C sample decreased during the first 200 cycles and increased afterward. This

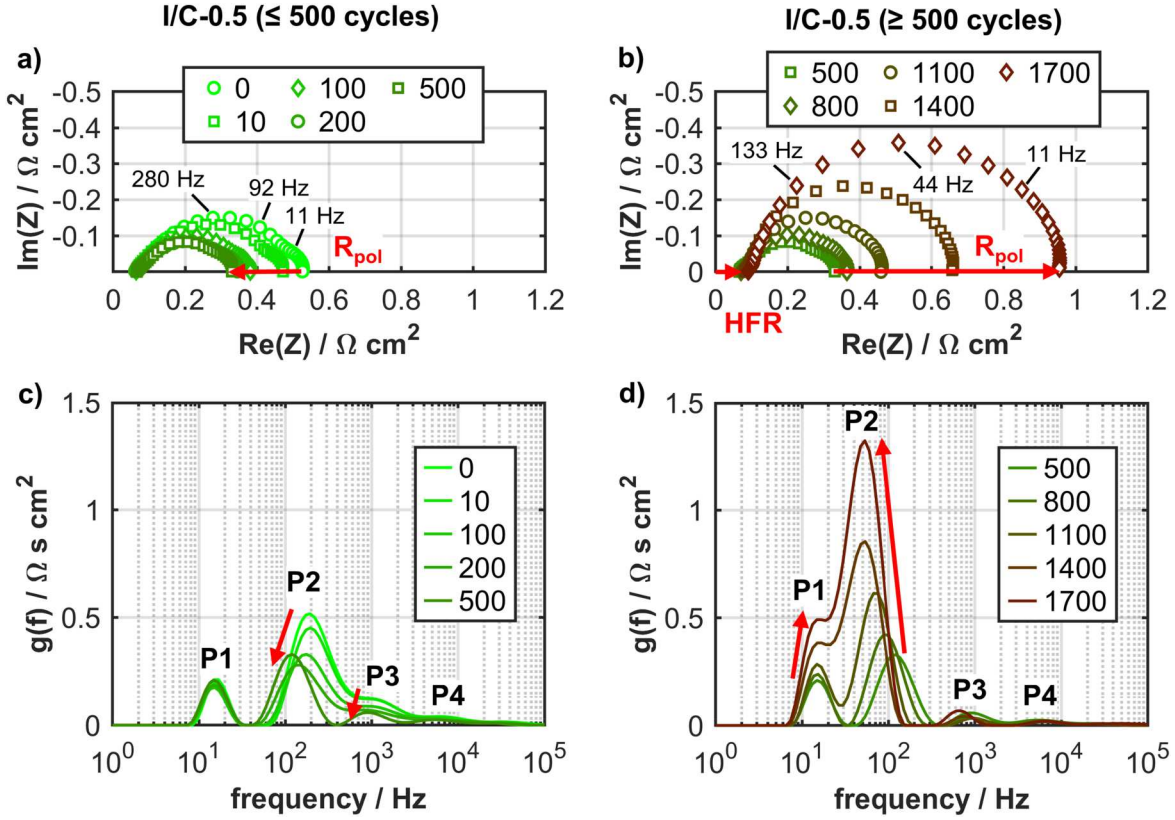

Figure 4. EIS (Nyquist plot) and distribution of relaxation times (DRT) of I/C-0.5 at 0.475 A cm^{-2} before (a, c), and after 500 (b,d) AST cycles (T = 80 °C; RH = 70% sym.; $p_{O2,dry}$ = 0.315 atm; $\dot{V}$ = 200 sccm).

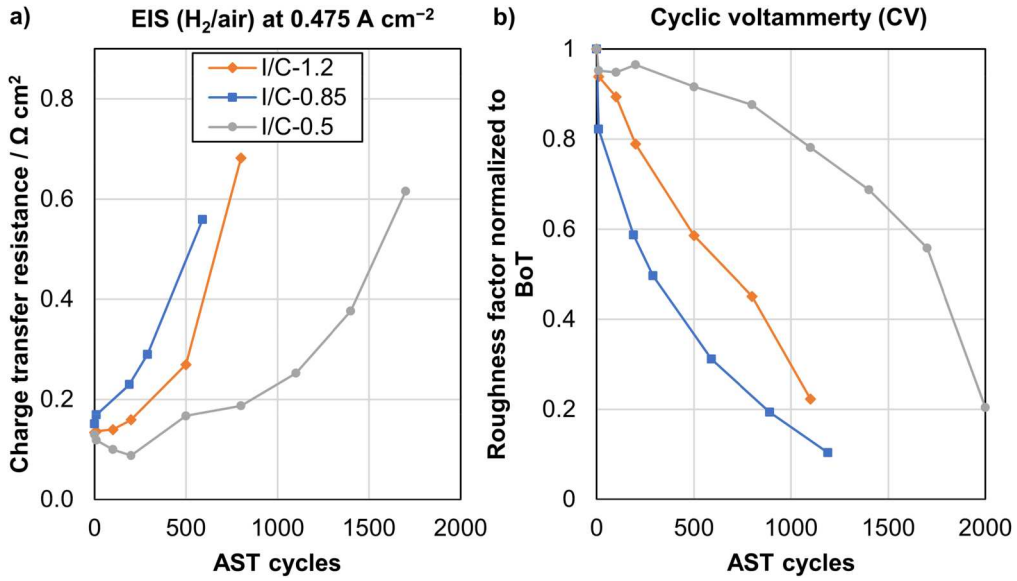

Figure 5. Charge transfer resistance at 0.475 A cm^{-2} (T = 80 °C; RH = 70% sym.; $p_{O2,dry}$ = 0.315 atm; $\dot{V}$ = 200 sccm) (a), and cathode roughness factor from cyclic voltammetry normalized to the BoT values (T = 50 °C; RH = 95% sym.; $\dot{V}$ = 200 sccm) (b) of all three I/C ratio samples (0.5/0.85/1.2) as a function of the AST cycles.

trend aligns well with the evolution of the **roughness factor and ECSA**, both of which remained stable up to 200 cycles. The cathode catalyst layer roughness factor, which describes the ratio of the electrochemically active platinum surface area and the geometrically active MEA area, was determined from the CVs (H-adsorption) and normalized to the BoT values of 111 cm^2_{pt} cm^{-2}_{geo} (I/C-1.2), 96 cm^2_{pt} cm^{-2}_{geo} (I/C-0.85), and 148 cm^2_{pt} cm^{-2}_{geo} (I/C-0.5). The roughness factor and ECSA of the medium and high I/C samples decrease steadily, which can be attributed to the detachment and agglomeration of platinum, as well as carbon corrosion and ionomer degradation.[74] However, these degradation mechanisms do not fully explain the initial behavior observed in the low I/C sample.

The **double-layer capacitance** (Fig. S7b) of the low I/C sample increased over the first 500 cycles before steadily decreasing. The double-layer capacitance, determined by CV, is dominated by the surface of carbon, platinum, and hydrophilic oxides that cover the carbon.[76] Here, the carbon surface contributes much more to the DLC than the platinum surface.[31] In addition, the water and ionomer at the carbon/Pt interface influence the DLC.[77] Higher ionomer coverage can mask electrochemically accessible carbon area and lower DLC,[78] whereas increased ionomer hydration and swelling can increase DLC.[79] The initial increase in DLC could be attributed to the formation of oxides on the carbon surface resulting from high potentials,[76] while the carbon corrosion leads to a subsequent decrease in DLC.[74,76]

Comparing the degradation rates of power density, ECSA, and charge transfer resistance in Table II, no clear correlation between the cathode I/C ratio and the degradation rates of these parameters could be identified. The observed differences can result from the differences in the CCL platinum loading (Table I).

Due to the initial performance improvement of I/C-0.5, its total degradation rate is lower than the rate calculated solely for the interval after 500 cycles alone. Nevertheless, both degradation rates are the lowest among all three samples.

Ionic resistance in the cathode catalyst layer.—The reduction in charge transfer resistance, as well as the stable cathode roughness factor (Fig. 5b) and ECSA (Fig. S9a), are key contributors to the initial performance increase observed from the low I/C sample. Furthermore, the decrease in peak P3 (Fig. 4c) from the DRT analysis, attributed to ionic resistance within the CCL, suggests an improvement in ionic conductivity.

In Fig. 6, the ionic resistance at three current densities is shown as a function of AST cycles. The ionic resistance decreases with increasing current density due to the increased water formation and humidification of the CCL.

The **ionic resistance in the CCL** at BoT is the highest for I/C-0.5 (0.401 Ω cm^2 at 0.475 A cm^{-2}), followed by I/C-0.85 (0.024 Ω cm^2) and I/C-1.2 (0.020 Ω cm^2). The lower resistance of the high I/C ratio sample can be attributed to a high ionomer volume fraction in the CCL, resulting in improved ionomer percolation and lower ionic resistance. The initially poor protonic conduction of I/C-0.5 may have inhibited carbon corrosion, resulting in lower initial carbon corrosion rates. However, we did not directly quantify carbon loss in this study, so this remains a hypothesis.

After 500 cycles, the ionic resistance of the low I/C sample (I/C-0.5) decreased from 0.401 Ω cm^2 (BoL) to 0.036 Ω cm^2, which is comparable to the BoT values of the medium and high I/C samples. The development of R_{ion} of I/C-0.5 was observed at all measured current densities (Fig. 6). One possible explanation for the initial

Table II. Degradation rates of power density, ECSA, and charge transfer resistance (R_{ct}) at 0.475 A cm^{-2} normalized to 1k AST cycles for the I/C ratio samples.

Cathode I/C ratio	Range of cycle number	Power density at 0.475 A cm^{-2} (%/1k cycles)	ECSA cathode (%/1k cycles)	R_{ct} at 0.475 A cm^{-2} (Ωcm^2/1k cycles)
0.5	BoL–EoL	−25	−20	+0.29
	500–EoL	−55	−35	+0.37
0.85	BoL–EoL	−106	−63	+0.69
1.2	BoL–EoL	−66	−64	+0.68

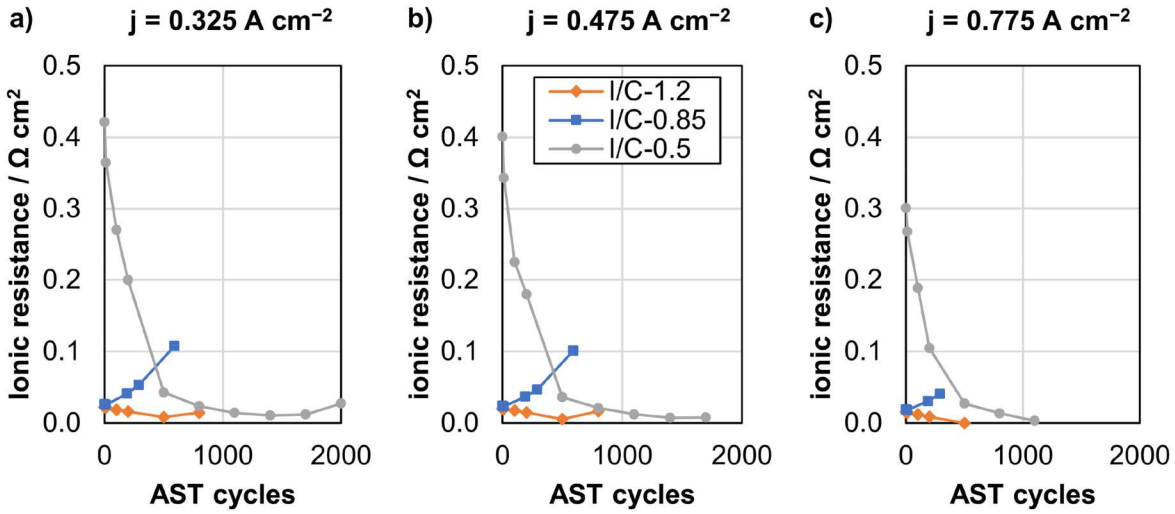

Figure 6. Ionic resistance in CCL at (a) 0.325 A cm^{-2}, (b) 0.475 A cm^{-2}, and (c) 0.775 A cm^{-2} of all I/C ratio samples (0.5/0.85/1.2) as a function of the AST cycles (T = 80 °C; RH = 70% sym.; $p_{O2,dry}$ = 0.315 atm; $\dot{V}$ = 200 sccm).

reduction in ionic resistance could be microstructural changes, such as the widening of the carbon micropore surface due to carbon corrosion, leading to improved connectivity through ionomer mobilization and redistribution.[66,80] Additionally, the high potentials could have led to a decreased hydrophobicity[81] of the carbon surface due to the formation of hydrophilic oxide surface groups[76,82] and an improved humidification by retained liquid water within the CCL, resulting in an increased ionic conductivity. Babu et al.[32] reported an initial performance increase in a high-surface-area carbon (HSAC) CCL (30PtA9029X, 30 wt% Pt, I/C: 0.77) during the first 200 cycles, though this improvement was not discussed in detail. In contrast, the low-surface-area carbon (LSAC/graphitized carbon) CCL (ElystPt200380, 20 wt% Pt, I/C: 0.77) exhibited stable performance with no significant changes until the end of the test (5000 cycles).[32] Given that both CCLs examined by Babu et al.[32] shared identical I/C ratios and differed solely in carbon type, it can be concluded that the observed initial performance improvement was primarily driven by the carbon support material and structure. These effects may stem from beneficial microstructural changes, which are more pronounced in high-surface-area carbon. The initial performance improvement observed at low I/C ratios may thus result from structural reorganization in the carbon support accompanied by improved proton connectivity within the catalyst layer. Additional targeted experiments, such as in situ microstructural analysis or dynamic humidity studies, are needed to further clarify the underlying mechanisms.

After 500 AST cycles, the ionic resistance of the low I/C sample (I/C-0.5) decreased moderately, a trend similar to the high I/C sample (I/C-1.2), which can be explained by a thinning of the CCL due to carbon corrosion, thereby decreasing the length of proton pathways. In contrast, the ionic resistance of the medium I/C sample (I/C-0.85) increased steadily with the AST cycle number. The opposite trends observed for I/C-0.85 and I/C-1.2 were confirmed by additional EIS measurements in H_2/N_2 (0.5 V, RH = 30%). However, the underlying reasons for this development remain unclear. The H_2/N_2 Nyquist plots (Fig. S10) and ionic resistances (Fig. S11) are provided in the supplementary material.

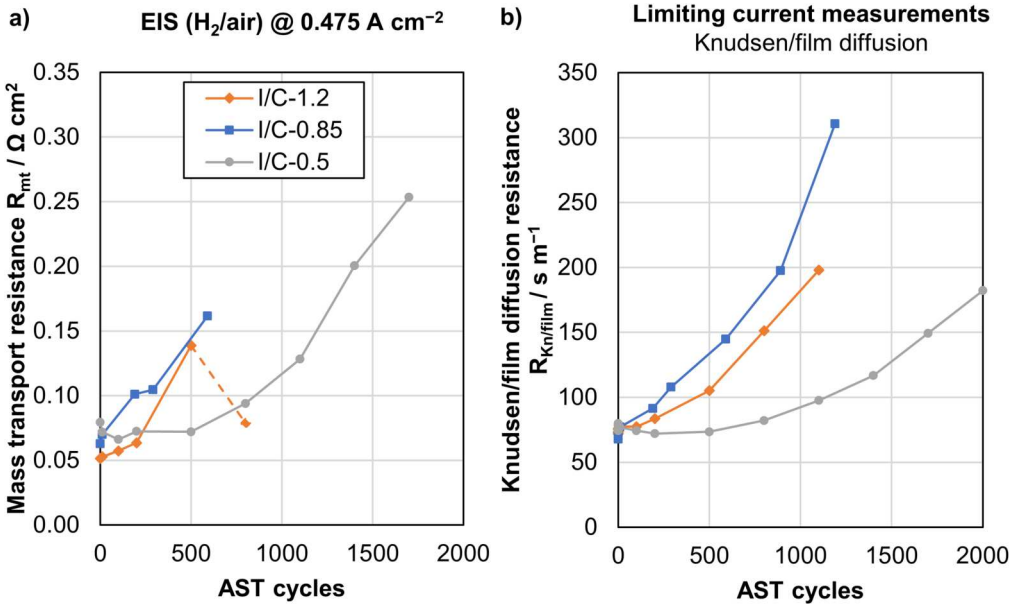

Figure 7. Total mass transport resistance at 0.475 A cm^{-2} from ECM fitting (T = 80 °C; RH = 70% sym.; $p_{O2,dry}$ = 0.315 atm; $\dot{V}$ = 200 sccm) (a), and Knudsen/film diffusion resistance from limiting current measurements (T = 80 °C; RH = 95% sym.; $\dot{V}$ = 200 sccm) (b) of all three I/C ratio samples (0.5/0.85/1.2) as a function of AST cycles.

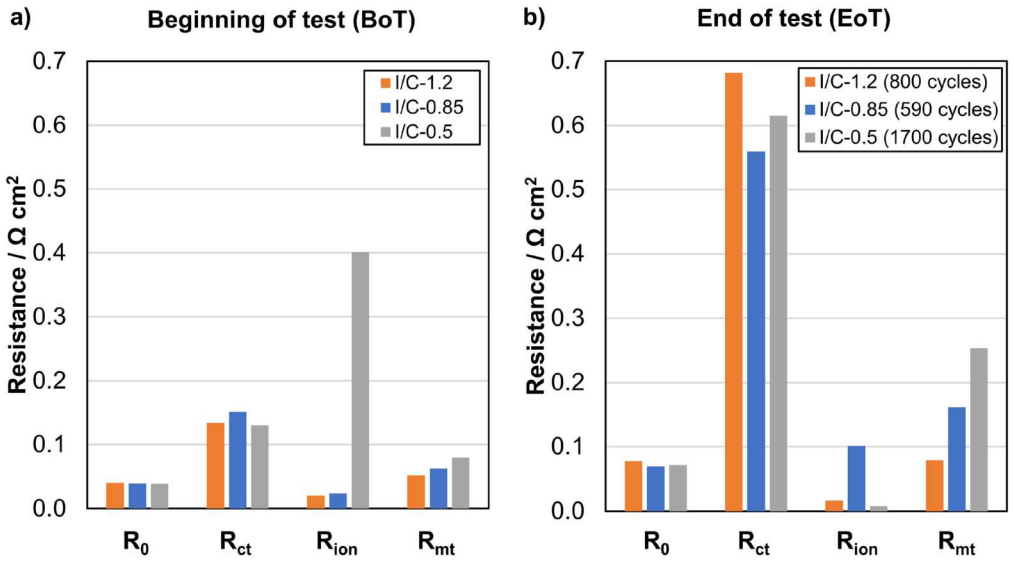

Figure 8. Comparison of all resistances at beginning of test (BoT) and end of test (EoT) at 0.475 A cm^{-2} (T = 80 °C; RH = 70% sym.; $p_{O2,dry}$ = 0.315 atm; $\dot{V}$ = 200 sccm).

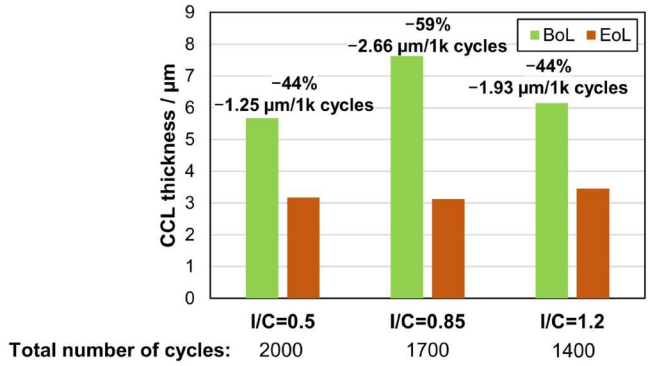

Figure 9. Cathode catalyst layer thicknesses of all three I/C samples at beginning of life (BoL) and end of life (EoL).

Mass transport resistance.—Mass transport resistances were determined by (i) hydrogen/air EIS coupled with DRT analysis and ECM fitting, yielding the low-frequency mass transport resistance R_{mt}, and by (ii) limiting-current measurements, providing the molecular oxygen diffusion resistance R_{mol} as well as the sum of the Knudsen and film diffusion resistance $R_{Kn/film}$. The mass transport resistance R_{mt}, obtained from the Warburg element within the ECM, represents oxygen transport across the GDL, MPL, and inactive regions of the CCL before reaching the ionomer-covered Pt/C surfaces. The molecular diffusion resistance R_{mol} originates predominantly from oxygen diffusion through the gas channel, GDL, and MPL, and to a minor extent, from the macropores in the CCL. In contrast, the Knudsen and film diffusion resistance $R_{Kn/film}$ describes transport limitations within the micropores of the MPL and CCL, as well as through the thin ionomer and water films surrounding the active reaction sites in the CCL.

In Fig. 7a, the total mass transport resistance (R_{mt}) determined by ECM fitting of the EIS (H_2/air) of all three I/C ratio samples is shown as a function of the AST cycles. Additionally, the development of the Knudsen and film diffusion resistance ($R_{Kn/film}$) is shown in Fig. 7b. The **molecular diffusion resistance** (R_{mol}) did not change significantly during AST cycling for the low and high I/C samples (Fig. S12), leading to the conclusion that the oxygen transport through the GDL is not affected by the ASTs. The increase of the medium I/C ratio at progressed corrosion states can be attributed to changes in the molecular diffusion in the CCL.

The **mass transport resistance** (R_{mt}) at BoT (Table SII) is in good accordance with the area under the DRT mass transport peak (P1) in Fig. 1d. The mass transport resistance decreases with an increasing I/C ratio from I/C-0.5 (0.079 Ω cm^2) to I/C-0.85 (0.063 Ω cm^2) and I/C-1.2 (0.051 Ω cm^2). The sharp increase in **mass transport resistance** (Fig. 7a) of the medium and high I/C samples can be attributed to a collapse of the carbon support structure leading to significant microstructural changes and a decrease in porosity,[2,83] indicated by a decrease in CCL thickness in Fig. 9. Furthermore, a decrease in pore size of the carbon support structure can impede mass transport to the reactive sites.[84] Additionally, a change in CCL thickness and additional liquid water can cause a shift in local current distribution and the penetration depth of protons in the catalyst layer.[8,22] For the low I/C sample, the sharp increase occurs only after 500 cycles, indicating that the reduced ionic resistance in the CCL leading to the initial performance increase did not affect the mass transport resistance.

The **Knudsen and film diffusion resistances** ($R_{Kn/film}$) at BoT are similar in magnitude for all samples with I/C-0.5 (80 s m^{-1}), I/C-1.2 (76 s m^{-1}), and I/C-0.85 (72 s m^{-1}). The value of I/C-1.2 and I/C-0.85 increased steadily with the AST cycles, with the rate of increase accelerating over time. In contrast, $R_{Kn/film}$ of I/C-0.5 remained stable until 500 cycles and then increased progressively afterward. This behavior of I/C-0.5 is in good agreement with the trend of mass transport resistance from ECM (R_{mt}). A recent study by Eppler et al.[66] found that platinum particles located in micropores contributed significantly more to total mass transport resistance than those situated outside the pores and in contact with ionomer. They also reported a significant increase of platinum in contact with ionomer from 30% to 85% during AST aging (H_2/N_2, 80 °C, 30k cycles, 0.6–0.95 V). This increase was attributed to platinum-catalyzed carbon corrosion, which caused the widening of micropores, ionomer redistribution, and ultimately a reduction in mass transport resistance.[66,80] Such microstructural changes could explain the observed decrease in ionic resistance within the CCL while maintaining stable mass transport resistance in the early stage of AST.

Figure 8 summarizes the resistances determined by EIS and ECM fitting at the beginning of test (BoT) and end of test (EoT) for all three I/C ratio samples at 0.475 A cm^{-2}.

At BoT (Fig. 8a), the ionic resistance (R_{ion}) is notably higher for the low I/C ratio (0.5), while charge transfer resistance (R_{ct}) and mass transport resistances (R_{mt}) are similar across all three I/C ratios. At EoT (Fig. 8b), substantial increases in R_{ct} and R_{mt} are observed

for all I/C ratios. These trends suggest that the initial differences in ionic resistance at low I/C ratios are overshadowed by the accelerated degradation of the carbon structure resulting in a increase in charge transfer and mass transport resistance. No clear correlation is observed between cathode I/C ratio and carbon corrosion behavior in the distribution of resistance before and after high-potential cycling ASTs.

Cross-section analysis.—The thicknesses of the cathode and anode catalyst layers, as well as the membrane, were measured at BoL and at EoL (Table SI). Figure 9 shows the thickness of the cathode catalyst layer for all three samples, which reduces significantly due to carbon corrosion. Although the samples vary slightly in their BoL values (5.7–6.8 μm), their EoL values showed a similar range (3.1–3.4 μm). Considering the total number of AST cycles, the rate of thickness reduction is highest for I/C-0.85 (−2.66 μm per 1000 cycles), followed by I/C-1.2 (−1.93 μm per 1000 cycles) and I/C-0.5 (−1.25 μm per 1000 cycles). Neglecting the first 500 cycles of I/C-0.5 results in a thinning rate of −1.67 μm per 1000 cycles, which is similar to the other two I/C ratio samples.

It is not quite clear to what extent the carbon structure of I/C-0.5 is corroded during the initial performance improvement up to 500 cycles. Since the reduction of CCL thickness is mainly attributed to the densification of the catalyst layer and, to a much smaller extent (<20%), to the loss of carbon mass,[2] the lower thinning rate of I/C-0.5 can be attributed to a delayed structural collapse of the carbon support. This hypothesis is supported by the later increase in mass transport resistance of I/C-0.5 (Fig. 7) in comparison to the other two samples. Additional experiments, such as online CO_2 detection to directly correlate carbon loss with electrochemical data, could help validate these findings.

Conclusions

This study systematically investigated the effect of the cathode catalyst layer ionomer-to-carbon (I/C) weight ratio on carbon corrosion behavior during high-potential cycling ASTs. MEAs with I/C ratios of 0.5, 0.85, and 1.2 were evaluated using a combination of diagnostic techniques, including electrochemical impedance spectroscopy, distribution of relaxation times, equivalent circuit/transmission line modeling, and additional electrochemical characterization methods such as cyclic voltammetry and limiting current measurements.

At BoL, the high I/C sample (I/C-1.2) achieved the highest performance, attributed to its low ionic resistance due to a higher ionomer volume fraction. In contrast, the low I/C sample (I/C-0.5) exhibited the poorest initial performance but showed a significant improvement of up to 35% during the first 500 high-potential cycles. This performance increase was correlated with a reduction in charge transfer resistance (∼ −37%) and ionic resistance in the CCL (−91%), likely due to microstructural rearrangements and improved ionomer connectivity under cycling conditions.

Despite its lower BoL power density, I/C-0.5 demonstrated superior durability, exhibiting the slowest degradation in charge transfer resistance, Knudsen/film diffusion resistance, and electrochemical surface area. These results suggest that low I/C layers may delay the onset of structural collapse within the CCL, providing a temporary suppression of carbon corrosion mechanisms.

Nevertheless, all samples eventually exhibited increases in ohmic resistance and declines in ECSA. Furthermore, the alignment in performance degradation trends for medium and high I/C samples indicates a shared structural failure mechanism, independent of initial ionic properties. The similar degradation trends of the medium and high I/C samples suggest that, at least for I/C ratios above 0.85, the carbon corrosion mechanisms during ASTs are not crucially affected by the cathode I/C ratio.

These findings underscore the importance of evaluating not only BoL performance but also long-term degradation behavior when optimizing the I/C ratio in CCL design. Future work should incorporate microstructural analysis to confirm the structural evolution during ASTs and to better assess how microstructural reorganization in low I/C ratios contributes to temporary performance recovery. Expanding the study to include a broader range of I/C ratios and alternative materials, such as short-side-chain ionomers,[85] highly oxygen-permeable ionomers (HOPIs),[86] or alternative carbon support like carbon nanofibers[87] and graphitized carbon supports,[88] could offer additional insights and new pathways for improving carbon corrosion resistance and mass transport properties.

Overall, these findings provide important guidance for the design of PEMFC catalyst layers, emphasizing the need to optimize ionomer content not only for initial performance but also for long-term structural stability and resistance to carbon corrosion.

Acknowledgments

The authors would like to thank the InnovationCampus Future Mobility (ICM), funded by the Baden-Württemberg Ministry of Science, Research, and Arts, Germany, for supporting Prof. Po-Ya Abel Chuang's research visit through the Future Mobility Grant program. The authors used ChatGPT-4o (OpenAI, https://openai.com) to assist with grammar and language review during the drafting of this manuscript. All content generated with the tool was critically reviewed and revised by the authors, who take full responsibility for the accuracy and integrity of the work.

ORCID

Sebastian Raab https://orcid.org/0009-0001-9031-4155
Ayon Karmakar https://orcid.org/0000-0002-9854-5185
Po-Ya Abel Chuang https://orcid.org/0000-0002-0440-1974
André Weber https://orcid.org/0000-0003-1744-3732

References

1. R. L. Borup, A. Kusoglu, K. C. Neyerlin, R. Mukundan, R. K. Ahluwalia, D. A. Cullen, K. L. More, A. Z. Weber, and D. J. Myers, *Curr. Opin. Electrochem.*, **21**, 192 (2020).
2. N. Macauley, D. D. Papadias, J. Fairweather, D. Spernjak, D. Langlois, R. Ahluwalia, K. L. More, R. Mukundan, and R. L. Borup, *J. Electrochem. Soc.*, **165**, F3148 (2018).
3. C. A. Reiser, L. Bregoli, T. W. Patterson, J. S. Yi, J. D. Yang, M. L. Perry, and T. D. Jarvi, *Electrochem. Solid-State Lett.*, **8**, A273 (2005).
4. R. Borup et al., *Chem. Rev.*, **107**, 3904 (2007).
5. H. Tang, Z. Qi, M. Ramani, and J. F. Elter, *J. Power Sources*, **158**, 1306 (2006).
6. L. Dubau et al., *WIREs Energy Environ.*, **3**, 540 (2014).
7. S. Komini Babu, D. Spernjak, J. Dillet, A. Lamibrac, G. Maranzana, S. Didierjean, O. Lottin, R. L. Borup, and R. Mukundan, *Appl. Energy*, **254**, 113659 (2019).
8. A. P. Young, J. Stumper, and E. Gyenge, *J. Electrochem. Soc.*, **156**, B913 (2009).
9. C. Cremers, T. Jurzinsky, J. Meier, A. Schade, M. Branghofer, K. Pinkwart, and J. Tübke, *J. Electrochem. Soc.*, **165**, F3307 (2018).
10. E. Niangar, T. Han, N. Dale, and K. Adjemian, *ECS Trans.*, **50**, 1599 (2013).
11. L. González Rodríguez, R. Andújar Lapeña, R. Campana Prada, G. Sevilla Toboso, and M. Sánchez Molina, *Fuel Cells*, **24**, e202200194 (2024).
12. X. Xie, G. Zhang, J. Zhou, and K. Jiao, *Int. J. Hydrogen Energy*, **42**, 12521 (2017).
13. M. Eguchi et al., *Polymers*, **4**, 1645 (2012).
14. N. Ramaswamy and J. Wortman, *ACS Energy Lett.*, **9**, 6170 (2024).
15. Y. Liu, M. W. Murphy, D. R. Baker, W. Gu, C. Ji, J. Jorne, and H. A. Gasteiger, *J. Electrochem. Soc.*, **156**, B970 (2009).
16. M. Okumura, Z. Noda, J. Matsuda, Y. Tachikawa, M. Nishihara, S. M. Lyth, A. Hayashi, and K. Sasaki, *J. Electrochem. Soc.*, **164**, F928 (2017).
17. R. Alink, R. Singh, P. Schneider, K. Christmann, J. Schall, R. Keding, and N. Zamel, *Molecules*, **25**, 1523 (2020).
18. S. Jeon, J. Lee, G. M. Rios, H.-J. Kim, S.-Y. Lee, E. Cho, T.-H. Lim, and J. Hyun Jang, *Int. J. Hydrogen Energy*, **35**, 9678 (2010).
19. P. Schneider, A.-C. Scherzer, B. D. Storey, M. Klingele, N. Zamel, and D. Gerteisen, *J. Electrochem. Soc.*, **170**, 104505 (2023).
20. K. Shinozaki, H. Yamada, and Y. Morimoto, *J. Electrochem. Soc.*, **158**, B467 (2011).
21. F. Du et al., *J. Electrochem. Soc.*, **167**, 144513 (2020).
22. J. P. Sabawa and A. S. Bandarenka, *Int. J. Hydrogen Energy*, **46**, 15951 (2021).
23. D. Lee and S. Hwang, *Int. J. Hydrogen Energy*, **33**, 2790 (2008).
24. G. Li and P. G. Pickup, *J. Electrochem. Soc.*, **150**, C745 (2003).
25. E. Passalacqua, F. Lufrano, G. Squadrito, A. Patti, and L. Giorgi, *Electrochim. Acta*, **46**, 799 (2001).
26. C.-M. Lai, J.-C. Lin, F.-P. Ting, S.-D. Chyou, and K.-L. Hsueh, *Int. J. Hydrogen Energy*, **33**, 4132 (2008).
27. M. R. Lee, H. Y. Lee, S. D. Yim, C. S. Kim, Y. G. Shul, A. Kucernak, and D. Shin, *Fuel Cells*, **18**, 129 (2018).

28. S. M. Andersen and L. Grahl-Madsen, *Int. J. Hydrogen Energy*, **41**, 1892 (2016).
29. A. D. Modestov, A. V. Kapustin, V. B. Avakov, I. K. Landgraf, and M. R. Tarasevich, *J. Power Sources*, **272**, 735 (2014).
30. M. Lopez-Haro, L. Guetaz, T. Printemps, A. Morin, S. Escribano, P. H. Jouneau, P. Bayle-Guillemaud, F. Chandezon, and G. Gebel, *Nat. Commun.*, **5**, 5229 (2014).
31. R. Alink, M. Schüßler, M. Pospischil, D. Erath, and D. Gerteisen, *J. Power Sources*, **327**, 526 (2016).
32. S. Komini Babu, R. Mukundan, C. Wang, D. Langlois, D. A. Cullen, D. Papadias, K. L. More, R. Ahluwalia, J. Waldecker, and R. Borup, *J. Electrochem. Soc.*, **168**, 044502 (2021).
33. U. S. Department of Energy, *The Fuel Cell Technologies Office Multi-Year Research, Development, and Demonstration Plan* (U. S. Department of Energy, Washington, DC) (2016).
34. M. F. Labata, G. Li, J. Ocon, and P.-Y. A. Chuang, *J. Power Sources*, **487**, 229356 (2021).
35. M. Heinzmann, A. Weber, and E. Ivers-Tiffée, *J. Power Sources*, **444**, 227279 (2019).
36. M. Heinzmann, A. Weber, and E. Ivers-Tiffée, *J. Power Sources*, **402**, 24 (2018).
37. Freudenberg Performance Materials GmbH & Co. KG, *Freudenberg Gas Diffusion Layers—Fuel Cell—Technical Data* (Freudenberg Performance Materials GmbH & Co. KG, Weinheim, Germany) (2025).
38. S. Mehrazi, T. Homayouni, N. Kakati, M. Sarker, P. Rolfe, and P.-Y. A. Chuang, *Appl. Energy*, **359**, 122680 (2024).
39. S. Kabir, D. J. Myers, N. Kariuki, J. Park, G. Wang, A. Baker, N. Macauley, R. Mukundan, K. L. More, and K. C. Neyerlin, *ACS Appl. Mater. Interfaces*, **11**, 45016 (2019).
40. M. Schönleber, D. Klotz, and E. Ivers-Tiffée, *Electrochim. Acta*, **131**, 20 (2014).
41. N. Wagner and K. A. Friedrich, *Fuel Cells*, **9**, 237 (2009).
42. M. Boillot, C. Bonnet, N. Jatroudakis, P. Carre, S. Didierjean, and F. Lapicque, *Fuel Cells*, **6**, 31 (2006).
43. D. Klotz, J. P. Schmidt, A. Kromp, A. Weber, and E. Ivers-Tiffée, *ECS Trans.*, **41**, 25 (2012).
44. M. Heinzmann and A. Weber, *J. Power Sources*, **558**, 232540 (2023).
45. J. F. V. Brichzin, H. Habermeier, G. Cristiani, and J. Maier, *Solid State Ion.*, **152–153**, 499 (2002).
46. J. Bisquert, *Phys. Chem. Chem. Phys.*, **2**, 4185 (2000).
47. D. Malevich, J. Pharoah, B. Peppley, and K. Karan, *ECS Trans.*, **41**, 721 (2011).
48. D. Malevich, B. R. Jayasankar, E. Halliop, J. G. Pharoah, B. A. Peppley, and K. Karan, *J. Electrochem. Soc.*, **159**, F888 (2012).
49. T. V. Reshetenko and J. St-Pierre, *J. Electrochem. Soc.*, **161**, F1089 (2014).
50. J. St-Pierre, *Fuel Cells*, **11**, 263 (2011).
51. K. C. Neyerlin, W. Gu, J. Jorne, A. Clark, and H. A. Gasteiger, *J. Electrochem. Soc.*, **154**, B279 (2007).
52. J. Song et al., *Chem. Eng. J.*, **496**, 153971 (2024).
53. H. Song, X. Shao, H. Zhang, P. Jiang, X. Wen, and Z. Zhan, *Int. J. Hydrogen Energy*, **67**, 282 (2024).
54. S. Du, S. Guan, S. Mehrazi, F. Zhou, M. Pan, R. Zhang, P.-Y. A. Chuang, and P.-C. Sui, *J. Electrochem. Soc.*, **168**, 114506 (2021).
55. M. S. Saha, D. Malevich, E. Halliop, J. G. Pharoah, B. A. Peppley, and K. Karan, *J. Electrochem. Soc.*, **158**, B562 (2011).
56. E. Brightman, G. Hinds, and R. O'Malley, *J. Power Sources*, **242**, 244 (2013).
57. S. Shahgaldi, I. Alaefour, and X. Li, *Appl. Energy*, **225**, 1022 (2018).
58. T. T. Ngo, T. L. Yu, and H.-L. Lin, *J. Power Sources*, **225**, 293 (2013).
59. Y. V. Yakovlev, Y. V. Lobko, M. Vorokhta, J. Nováková, M. Mazur, I. Matolínová, and V. Matolín, *J. Power Sources*, **490**, 229531 (2021).
60. Q. Xue, R. Zhang, D. Yang, B. Li, P. Ming, and C. Zhang, *Int. J. Hydrogen Energy*, **47**, 23335 (2022).
61. T. Soboleva, K. Malek, Z. Xie, T. Navessin, and S. Holdcroft, *ACS Appl. Mater. Interfaces*, **3**, 1827 (2011).
62. K. Park, R. Gao, M. So, T. H. Noh, N. Kimura, Y. Tsuge, and G. Inoue, *J. Power Sources Adv.*, **15**, 100096 (2022).
63. T. Soboleva, X. Zhao, K. Malek, Z. Xie, T. Navessin, and S. Holdcroft, *ACS Appl. Mater. Interfaces*, **2**, 375 (2010).
64. A. Weber, *Fuel Cells*, **21**, 440 (2021).
65. J. N. Soderberg, A. C. Co, A. H. Sirk, and V. I. Birss, *J. Phys. Chem. B*, **110**, 10401 (2006).
66. M. Eppler, M. Hanauer, U. Berner, V. Leduc, T. Kadyk, and M. H. Eikerling, *J. Electrochem. Soc.*, **172**, 054509 (2025).
67. S. Ott, A. Orfanidi, H. Schmies, B. Anke, H. N. Nong, J. Hubner, U. Gernert, M. Gliech, M. Lerch, and P. Strasser, *Nat. Mater.*, **19**, 77 (2020).
68. S. Shukla, F. Wei, M. Mandal, J. Zhou, M. S. Saha, J. Stumper, and M. Secanell, *J. Electrochem. Soc.*, **166**, F1142 (2019).
69. Z. Yu, R. N. Carter, and J. Zhang, *Fuel Cells*, **12**, 557 (2012).
70. S. Salari, J. Stumper, and M. Bahrami, *Int. J. Hydrogen Energy*, **43**, 16704 (2018).
71. H. Oh, Y. i Lee, G. Lee, K. Min, and J. S. Yi, *J. Power Sources*, **345**, 67 (2017).
72. A. Orfanidi, P. J. Rheinländer, N. Schulte, and H. A. Gasteiger, *J. Electrochem. Soc.*, **165**, F1254 (2018).
73. P. Gazdzicki, J. Mitzel, A. M. Dreizler, M. Schulze, and K. A. Friedrich, *Fuel Cells*, **18**, 270 (2017).
74. R. Sharma and S. M. Andersen, *ACS Catal.*, **8**, 3424 (2018).
75. J. Kwon, P. Choi, S. Jo, H. Oh, K.-Y. Cho, Y.-K. Lee, S. Kim, and K. Eom, *Electrochim. Acta*, **414**, 140219 (2022).
76. A. P. Young, V. Colbow, D. Harvey, E. Rogers, and S. Wessel, *J. Electrochem. Soc.*, **160**, F381 (2013).
77. H. Iden and A. Ohma, *J. Electroanal. Chem.*, **693**, 34 (2013).
78. Y. Chen, Q. Zhong, G. Li, T. Tian, J. Tan, and M. Pan, *Ionics*, **24**, 3905 (2018).
79. A. Perego, A. Avid, D. N. Mamania, Y. Chen, P. Atanassov, H. Yildirim, M. Odgaard, and I. V. Zenyuk, *Appl. Catal. B: Environ.*, **301**, 120810 (2022).
80. L. Amichi, H. Yu, A. Ziabari, O. Rahman, D. Arregui-Mena, L. Hu, K. C. Neyerlin, and D. A. Cullen, *Adv. Energy Mater.*, **14**, 2402310 (2024).
81. X. Zhang, Y. Yang, L. Guo, and H. Liu, *Int. J. Hydrogen Energy*, **42**, 4699 (2017).
82. Z. Zhao, L. Castanheira, L. Dubau, G. Berthomé, A. Crisci, and F. Maillard, *J. Power Sources*, **230**, 236 (2013).
83. Z. Fang, A. G. Star, and T. F. Fuller, *J. Electrochem. Soc.*, **166**, F709 (2019).
84. H. Schulenburg, B. Schwanitz, N. Linse, G. G. Scherer, A. Wokaun, J. Krbanjevic, R. Grothausmann, and I. Manke, *J. Phys. Chem. C*, **115**, 14236 (2011).
85. K. Talukdar, P. Gazdzicki, and K. A. Friedrich, *J. Power Sources*, **439**, 227078 (2019).
86. J. Liu and S. Litster, *J. Electrochem. Soc.*, **172**, 034508 (2025).
87. M. Sung, H. Yi, J. Han, J. B. Lee, S. H. Yoon, and J. I. Park, *Membranes*, **15**, 3 (2024).
88. Q. Xue, J. B. Huang, D. J. Yang, B. Li, and C. M. Zhang, *RSC Adv.*, **11**, 19417 (2021).